Materials Advances

PAPER

Check for updates

Shrimp shell-derived chito-protein nanocomposites for sustainable dye effluent remediation: efficiency, reusability, and environmental safety

Nisrine Nouj, [ID] *[a] Zineb Majbar,[b] Ingrid Ioana Buciscanu,[c] Aboubakr Ben Hamou, [ID] [a] Ayoub Chaoui,[a] Mohamed Rida Abelouah,[d] Mohamed Idbella,[e] Abdelaziz Ait Addi,[f] Nadia Eladlani,[g] Ali Zourif, [ID] [h] Mohamed Benafqir, [ID] [a] Naima Hafid,[a] Igor Cretescu,[i] Amane Jada[j] and Noureddine El Alem[a]

The transformation of seafood processing residues into advanced functional materials offers a dual solution to environmental pollution: mitigating waste streams while addressing water contamination. In this study, shrimp exoskeletons were valorized into a chitin–protein composite (SE-CP) through acid demineralization and thermal activation and evaluated as a biosorbent for the removal of anionic textile dyes Sellacid Red (SR) and Sellaset Blue (SB). The material was characterized using SEM, EDX, FTIR, XRD, BET, DLS, XPS, and PZC analyses, confirming a mesoporous structure (specific surface area = 51.4914 m^2 g^{-1}) enriched with amino and hydroxyl groups that favor electrostatic and hydrogen-bonding interactions. Batch adsorption studies showed maximum removal efficiencies of 99.2% for SR at pH = 3 and 98.7% for SB at pH = 4 both around 20 °C and an initial dye concentration of 100 mg L^{-1}. Kinetic data fitted the pseudo-second-order model ($R^2 > 0.96$), and equilibrium was best described by the Freundlich isotherm, with adsorption capacities of 158.43 mg g^{-1} (SR) and 63.81 mg g^{-1} (SB). SE-CP retained over 76% of its adsorption capacity after five regeneration cycles, indicating strong stability and reusability. This work demonstrates a low-cost and sustainable biosorbent derived from shrimp waste, with high efficiency, reusability, and green synthesis, positioning SE-CP as a promising candidate for industrial dye wastewater treatment within circular economy principles.

^{a} *Laboratory of Materials and Environment (LME), Faculty of Sciences, Ibn Zohr University, Agadir, Morocco. E-mail: n.nouj@uiz.ac.ma, nouj.nisrine@gmail.com*

^{b} *Engineering, Electrochemistry and Modeling Environment Laboratory (LEEME), Faculty of Sciences, Sidi Mohamed Ben Abdellah University, Fez 30000, Morocco*

^{c} *Department of Chemical Engineering in Textiles and Leather, Faculty of Industrial Design and Business Management, "Gheorghe Asachi" Technical University of Iasi, Iasi 700050, Romania*

^{d} *Laboratory of Aquatic Systems: Marine and Continental Environments, Faculty of Sciences, Ibn Zohr University, Agadir 80000, Morocco*

^{e} *College of Agriculture and Environmental Sciences, AgroBioSciences (AgBS) program, Mohammed VI Polytechnic University, Ben Guerir 43150, Morocco*

^{f} *Physical Chemistry & Environment Team, Faculty of Sciences, Ibn Zohr University, Agadir, Morocco*

^{g} *Interdisciplinary Laboratory in Bio-Resources, Environment and Materials, Higher Normal School, Cadi Ayyad University, 4000 Marrakech, Morocco*

^{h} *Laboratory of Physical-Chemistry, Materials and Catalysis, Faculty of Sciences Ben M'sick, Hassan II University of Casablanca, Morocco*

^{i} *Department of Environmental Engineering and Management, Faculty of Chemical Engineering and Environmental Protection, "Gheorghe Asachi" Technical University of Iasi, Iasi 700050, Romania*

^{j} *Institute of Materials Science of Mulhouse (IS2M), High Alsace University, Mulhouse 68100, France*

1. Introduction

Global socio-economic development and population growth over the last few decades have led to an increase in the quantity and qualitative complexity of special wastes generated by the industrial sector.[1,2] However, the global fishing industry generates over 20 million tons of by-products every year, almost all of which is simply wasted.[3,4] After processing, 25% of the total ends up as waste, including fish species that were not intended to be caught or other remnants of industrial fish processing.[3,5] These marine by-products are generally discarded without taking into account their precious compositions which can be used as value-added products. A large number of fish processing units generate both a large quantity of co-products (bones, skins, scales, fins and swim bladders, which represent 36%, or even 60%, of the mass of raw materials[3,6]) and a large quantity of untreated wastewater.[7,8] Therefore, recovering this waste and transforming it into valuable products are becoming important

ways leading to solid waste remediation and taking advantage of the marine products and bio-resources.

It should be noted that chitin is an abundant biological polymer, particularly in marine animals and insects.[9,10] The crystalline chitin fiber has good properties that enable it to serve as a load-bearing scaffold for the entire bio-composite material, and the other component is usually a protein.[11] The remarkable affinity occurring between chitin and proteins is probably one of the main reasons explaining the presence of such a composite in nature.[12] Many biological materials, including the exoskeleton of sponges, the cuticles of crustaceans and insects, the beaks of squid, cuttlefish bones and the fangs of spiders, are made up of chitin and protein complexes.[13] These chitin–protein complexes exhibit a variety of mechanical behaviours and perform multiple functions, depending on the species and even the different body parts of the same species.[14] The use of the chito-protein complex as a biosorbent remains a challenge, given that chitosan is the main biological substance in these fields. However, chitosan exhibits a little solubility in water, under neutral or alkaline conditions. These factors limit the biopolymer feasibility, in addition to its complicated extraction process.[15,16] Hence, there is a need to find alternative ways to minimize the biopolymer extraction process and preserve its contaminant-removal properties, particularly for dyes.

The most widespread contaminants found in the textile industry are the cheapest dyes, which are harmful to human health and contribute to environment degradation.[17] This low cost of these dyes results from their easy synthesis process, mainly for azo dyes, and the possibility of obtaining a wide palette of colors and shades.[18] Thus, despite their toxicity, little research has been carried out taking into account this issue. Hence, Acid red 337 (Sellacid Red PF) and the 1 : 2 chromium complex of Acid Blue 349 (Sellaset Blue H) belonging to this group of azo dyes are widely used in the textile industry. Furthermore, Acid red 337 has been registered by the European Chemicals Agency (ECHA) as an organic compound harmful to the aquatic environment, and Acid Blue 349 presents similar risks. Therefore, their treatment by using low-cost biosorbents based on fish waste will reduce the risk to human health and avoid the environmental issue.

In the present work, shrimp shells were modified for their use as a biosorbent to remove hazardous low-cost dyes from aqueous solutions. The focus was on the powder, in order to assess its effectiveness in removing two categories of dyes: low- and high-molecular-weight anionic dyes. The shrimp shell modification consisted of the powder extraction after the raw by-product demineralization process. Regarding the toxic dyes, aqueous solutions containing two different anionic dyes were treated by using the bio-based sorbent, in batch equilibrium biosorption tests. A combination of techniques was used to study biosorption mechanisms.

The aim of the present work is to prepare a value-added, bio-based biosorbent suitable for the dye-contaminated effluent treatment. Thus, a biosorbent from renewable resources, offering excellent dye sorption and desorption performance, even at high dye concentrations, for repeated, high-speed dye removal, was developed. Indeed, the objective of our study falls within the framework of three Sustainable Development Goals (SDGs): No. 6, No. 14 and No. 15: improve wastewater treatment and reuse (No. 6) and protect the aquatic environment (No. 14) and the terrestrial environment (No. 15) from persistent chemical substances present in wastewater after treatment with reclaimed marine waste.

2. Materials and experimental methods

2.1. Chemicals

HCl, $NaNO_3$, HNO_3 and NaOH were of analytical grade and purchased from Sigma Aldrich. Sellacid Red PF and Sellaset Blue H were sourced from TFL Ledertechnik GmbH, Germany. Distillated water (DW) was used for all aqueous solutions.

2.2. Preparation of the biosorbent

Shrimp (*Parapenaeus longirostris*) exoskeletons were purchased from a local market in Agadir city, Morocco. The exoskeletons were first washed with tap water and then several times with distilled water to remove any foreign debris. The resulting shells were dried at 220 °C for 15 min, ground and sieved to a size of about 500 μm. Thereafter, the resulting material was treated with 1 M HCl in a shrimp shell to HCl solution ratio of 1 : 10 (w/v) for 30 min to remove the mineral constituent (calcite $CaCO_3$). The obtained biosorbent (SE-CP) was washed and filtered to a neutral pH, then dried at 105 °C to constant weight and finally stored for use.
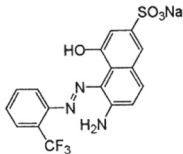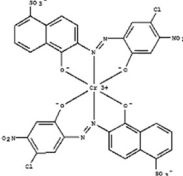
2.3. Sorbate investigation

Two commercial dyestuffs, Sellacid Red PF and Sellaset Blue H (TFL Ledertechnik GmbH, Germany) currently used for wool and leather dyeing, were the adsorbates studied in this paper. The structural formulas, molecular weights, maximum absorbance wavelengths, and commercial and C.I. names of the two acid dyes are given in Table 1. A stock solution of each dye (1000 mg L^{-1}) was prepared and diluted to the initial concentrations required for the sorption and kinetics studies. Hydrochloric acid (0.1 M) and sodium hydroxide (0.1 M) were used to adjust the pH of the solutions. All solutions were prepared with DW, and the handled reagents were of analytical grade.

2.4. Biosorbent characterization

Various characterization methods were used to assess the morphology, structure, composition and sorption properties of SE-CP. Thus, the morphological characteristics were obtained using scanning electron microscopy (SEM) (SEM, JEOL, JSM-IT200, Akishima, Tokyo, Japan). The elemental composition was determined using energy dispersive X-ray (EDX) analysis. Fourier transform infra-red (FTIR) spectroscopy spectra were recorded in the 4000–500 (cm^{-1}) range using attenuated total reflection Fourier transform infrared spectroscopy (ATR-FTIR, SHIMADZU, IRAffinity-1S, Paris, France). The crystalline structure of the biosorbent was determined by using

Table 1 The main characteristics of tested dyes

Structural formula	Commercial name	Color index (C.I.) name	λ_{max}, nm	pK_a	M_W, g mol^{-1}
	Sellacid Red PF	Acid Red 337	500	6.5	433.34
	Sellaset Blue H	(1:2 chromium complex) of Acid Blue 349	590	0.5	943.53

X-ray diffraction (Bruker D8 Twin, Jena, Germany). The biosorbent specific surface area and the mean pore volume were assessed by the Brunauer–Emmett–Teller (BET) adsorption method using a Micrometrics analyzer, an ASAP 2020 instrument. X-ray photoelectron spectroscopy (XPS VG SCIENTA, model SES-200) was used to assess the structure and composition of the studied biosorbent.

2.5. Properties of aqueous biosorbent suspension

2.5.1. pH of the biosorbent aqueous suspension. The pH of the biosorbent aqueous suspension was adjusted to an initial pH between 2 and 10 by using aqueous solutions of HNO$_3$ (0.1 M) and NaOH (0.1 M). Then, the mixtures were stirred for 24 hours (to ensure homogenization of the suspension) at 250 rpm until the pH became constant. All experiments were carried out in a tank thermostatic bath at 20 ± 0.2 °C.

2.5.2. Surface electrical properties of biosorbent aqueous suspension. Regarding the biosorbent surface electrical properties, the point of zero charge (PZC) was determined using a titration method consisting in addition of amounts of dye to aqueous solution.[19] Using this method, an aqueous suspension of biosorbent was first prepared by mixing 0.2 g of the biosorbent with a total volume of 40 mL of NaNO$_3$ (0.1 M). Thereafter, the resulting biosorbent aqueous suspension was titrated with the aqueous dye solution by using a Mütek PCD 02 device for measuring standard induced potential (SIP).[20] The device used consists of a cylindrical tube and a poly(tetrafluoroethylene) piston. The SIP is measured between two electrodes placed at opposite ends of the chamber. This potential mainly describes the electrostatic interactions occurring between the negative and positive surface sites produced between the dye and the biosorbent, respectively. The resulting SIP was then normalized to its maximum value.

2.5.3. Particle size of the biosorbent aqueous dispersion. Measurements of the biosorbent particle size dispersed in aqueous media were carried out using dynamic light scattering (DLS). The instrument used is a Coulter Model N4S (Coultronics), operating with a 4 mW helium-neon laser at a wavelength of 632.8 nm.[20]

2.6. Batch sorption experiments

Batch equilibrium sorption experiments were performed as a function of various parameters such as the dye concentration, the biosorbent dosages, the aqueous phase pH, the adsorbate–adsorbent contact time, and the suspension temperature.

Specifically, the biosorption experiment was conducted in a set of glass vials containing different initial dye concentrations (25, 50, 75, 100, 125, 150, 200, 250, 300, and 350 mg L^{-1}) at different pH values (2–12) using different biosorbent dosages (0.02, 0.04, 0.06, 0.08, 0.1, 0.12, 0.14, 0.16, 0.18, 0.2 g) for periods of 15, 30, 60, 120, and 240 min, and temperature values of 20, 30 and 40 °C. Also, the pH was adjusted to the desired values with 0.1 mol L^{-1} HCl or 0.1 mol L^{-1} NaOH solutions. However, the measurements before and after the process were taken using a pH meter (OHAUS Starter 2100 pH meter).

After treatment, the supernatant was withdrawn after 24 h of decantation to measure the residual concentration of both dyes in the solution using an UV-Vis spectrophotometer (U-2910, Hitachi, USA). Standard curves of absorbance and linear regression equations had been previously obtained for both colorants. Each kinetic experiment was performed for each dye solution in triplicate. The biosorption capacity for each time interval was calculated using eqn (1):

$$q_t = \frac{(C_i - C_t)V}{m_b} \tag{1}$$

where C_i (mg L^{-1}) is the initial dye concentration, C_t (mg L^{-1}) is the dye concentration at a given treatment time (including the equilibrium moment), V (L) is the volume of the dye solution, and m_b (g) is the mass of sorbent added to the solution. Finally, the dye removal was calculated using eqn (2):

$$\text{Removal rate (\%)} = \frac{(C_0 - C_t)}{C_i} \times 100\% \tag{2}$$

where C_0 and C_t represent the initial and final (after biosorption) dye concentrations, respectively. All tests were performed in triplicate, and the data reported reflect the average of the triplicate measurements.

2.7. Biosorption theory

2.7.1. Equilibrium isotherms. Three isothermal equilibrium models (Langmuir, Freundlich and Elovich) were used to study the behavior of the SE-CP surface during the biosorption process. To demonstrate that the sorbent surface is uniform and homogeneous, the Langmuir isotherm was used, where the sorbates are bound in a monolayer. The active sites of the biosorbent should be morphologically similar when applying the following equation:[21]

$$q_e = \frac{C_e K_L Q_{max}}{1 + C_e K_L} \tag{3}$$

where q_e is the equilibrium biosorption capacity, C_e is the equilibrium concentration (mg L^{-1}), Q_{max} corresponds to the theoretical maximum monolayer biosorption capacity (mg g^{-1}) and K_L is the Langmuir isothermal constant (L mg^{-1}).

A multilayer formation of the solid sorbate on the sorbent surface requires an application of the Freundlich isotherm. At the same time, the model is formulated in an exponential form as shown in the following equation:[21]

$$q_e = K_F C_e^{1/n} \tag{4}$$

where K_F ((mg g^{-1})(L mg^{-1})$^{1/n}$) is the Freundlich isotherm constant related to adsorption capacity, and n is the biosorption intensity factor.

The Temkin isotherm shows whether the sorption phenomenon is based on a linkage factor with an assumption of decreasing biosorption heat with increasing sorbent surface coverage by sorbate particles. The model has a nonlinear form, as presented in the following equation:[21]

$$q_e = \frac{RT}{b} \times \ln(K_T C_e) \tag{5}$$

where R, T, K_T, and b are the universal gas constant (J mol^{-1} K), adsorption equilibrium constant (K), Temkin' isothermal constant (L mg^{-1}), and the binding factor related to the heat of biosorption (K).

2.7.2. Kinetic models. Kinetic modeling was used to examine the dynamics of the biosorbent using pseudo-first order, pseudo-second order, and intra-particle diffusion kinetic models. The pseudo-first-order kinetic model focuses on localized biosorbent sites filled with sorbate molecules in the absence of interactions. This model is represented by the following equation:[21]

$$q_t = q_{e,the}(1 - \exp^{k_1,t}) \tag{6}$$

where $q_{e,the}$, k_1, and t are the theoretical biosorption capacity (mg g^{-1}), rate constant for the pseudo-first-order model (min^{-1}), and time (min), respectively.

The pseudo-first-order kinetic model is described by a second-order rate equation as specified and represented in the following equation:[21]

$$q_t = \frac{k_2 q_{e,the}^2 t}{1 + k_2 q_{e,the} t} \tag{7}$$

where k_2 is the rate constant for the pseudo-second-order model (mg g min^{-1}).

The kinetic model for intra-particle diffusion is formulated based on internal diffusion which is the rate limiting step with an account for external mass transfer effects. The model is described by the following equation:[21]

$$q_t = k_d t^{1/2} + Q_0 \tag{8}$$

where k_d is the rate constant for the intra-particle diffusion model (mg min$^{1/2}$ min^{-1}) and Q_m is the instantaneous biosorption capacity of the sorbent at time zero (mg g^{-1}).

2.7.3. Biosorption thermodynamics. The biosorption capacity of the SE-CP was studied at different temperatures of 20, 30, 40 and 50 °C under optimized conditions.

Three thermodynamic parameters were selected using the proper biosorption capacity (q_e) and the experimental equilibrium solution concentration (C_e). Gibb's free energy (ΔG), the change in enthalpy (ΔH) and the change in entropy (ΔS) were obtained using the following equations:[21]

$$\Delta G = -RT \times \ln\left(\frac{q_e}{C_e}\right) \tag{9}$$

where the values of ΔH and ΔS are obtained from the slope and intercept provided by the linear plot between the distribution coefficient $\ln(q_e/C_e)$ and $(1/T)$.

$$\ln\left(\frac{q_e}{C_e}\right) = \frac{\Delta S}{R} - \frac{\Delta H}{RT} \tag{10}$$

At constant temperature, the ΔG is calculated as a function of the heat of biosorption and the entropy change using the following equation:

$$\Delta G = \Delta H - T\Delta S \tag{11}$$

2.8. Biosorbent regeneration experiments

Following sorption equilibrium, regeneration of the biomaterial used was carried out with two desorption agents: distilled water (DW) and NaOH (0.1 M), in order to assess their desorption efficiency and the reusability of the dye-loaded biosorbent. The experimental regeneration protocol involves immersing the loaded adsorbent in NaOH or DW (0.1 g/100 mL) for 4 hours, followed by a DW wash. Then, the regenerated SE-CP was dried in an oven at 105 °C. Finally, the regenerated materials (SE-CP@OH and SE-CP@DW) were reused for further biosorption tests. The regeneration process was repeated several times to achieve complete dye removal. SE-CP@OH and SE-CP@DW were thoroughly washed with distilled water to neutral pH and then reused in biosorption experiments four times using the same biosorbents. According to data, sorbent regeneration mass yield was calculated to assess the durability of the material used, which can be calculated using equation:[22]

$$\text{Mass recovery yield (\%)} = \frac{m_{e,\text{regenerated}}}{m_{e,\text{fresh}}} \times 100\% \tag{12}$$

where $m_{e,regenerated}$ and $m_{e,fresh}$ are the mass of regenerated and fresh adsorbent, respectively.

3. Results and discussion

3.1. Full characterization of SE-CP

3.1.1. Main chemical elements in the biosorbent as assessed by the XPS method. X-Ray photoelectron spectroscopy was used to perform a quantitative elemental analysis and examine the surface composition of SE-CP. This technique specifically assessed the presence of three key elements carbon (C), oxygen (O), and nitrogen (N) that are fundamental to the α-chitin–protein nanofibers expected in the biosorbent.

The XPS wide-scan results (Fig. 1(a)) indicate a high carbon content of 74.2%, consistent with chitin being the primary biopolymer in the material. Oxygen and nitrogen were detected at 18.8% and 6.9%, respectively, due to the presence of primary and secondary amides. To further investigate the chemical binding states of these elements, high-resolution XPS spectra were analyzed. The carbon spectrum (Fig. 1(b)) was deconvoluted into three peaks at 284.8 eV, 284.13 eV, and 285.92 eV, corresponding to C–C/C–H, C–N, and C=O, respectively.[23] However, we acknowledge the reviewer's concern regarding the calibration of binding energy (BE). While a BE of 284.8 eV is commonly assigned to C–C/C–H bonds, the shift in our data may stem from surface charging effects or the specific nature of the SE-CP material. Similarly, the oxygen spectrum (Fig. 1(c)) exhibited three deconvoluted peaks at 529.21 eV, 530.10 eV, and 531.45 eV, assigned to carbonyl, ether, and carboxyl-type oxygen species, respectively. The nitrogen spectrum (Fig. 1(d))

revealed three peaks at 387.18 eV, 397.88 eV, and 398.96 eV, corresponding to pyridinic-N, pyrrolic-N, and graphitic-N, respectively.[24] The presence of these nitrogen configurations suggests structural modifications induced by the acid treatment rather than pyrolysis. Thus, the *in situ* modification of the biosorbent SE-CP, as described in Section 2.2, leads to generation of pyridinic and pyrrolic nitrogen types associated with oxygen-containing groups. These groups introduce, in turn, more active sites, leading to additional sorption efficiency of the biosorbent SE-CP. As expected, all these functional groups have been attributed to the presence of proteins and polysaccharides.[23] It should be noted that the nitrogen present on the surface of the biosorbent SE-CP results from the reaction between the amino group and the hydroxide group during the demineralization step consisting in the mineral layer removal from the raw shrimp exoskeleton. Moreover, the presence of pyridinic nitrogen and pyrrolic nitrogen elements as evidenced by the XPS results (Fig. 1(d)) will play an important role in enhancing the nanoporosity of SE-CP, thereby increasing the number of active sites. In addition, the bond breaking produces long-chain carboxylic acids, ketones and aldehyde groups which react with –NH and –NH2 to generate amino intermediates, which then condense to produce pyridines and pyrimidines. These findings are in good agreement with other reported works confirming that the graphitic nitrogen element present in the SE-CP biosorbent exhibits higher biosorption activity and stability than other nitrogen configurations.

3.1.2. Surface area and porosity of the SE-CP biosorbent as determined by the BET method. Adsorption–desorption isotherms for N_2 for the SE-CP biosorbent, measured at 77° K, are
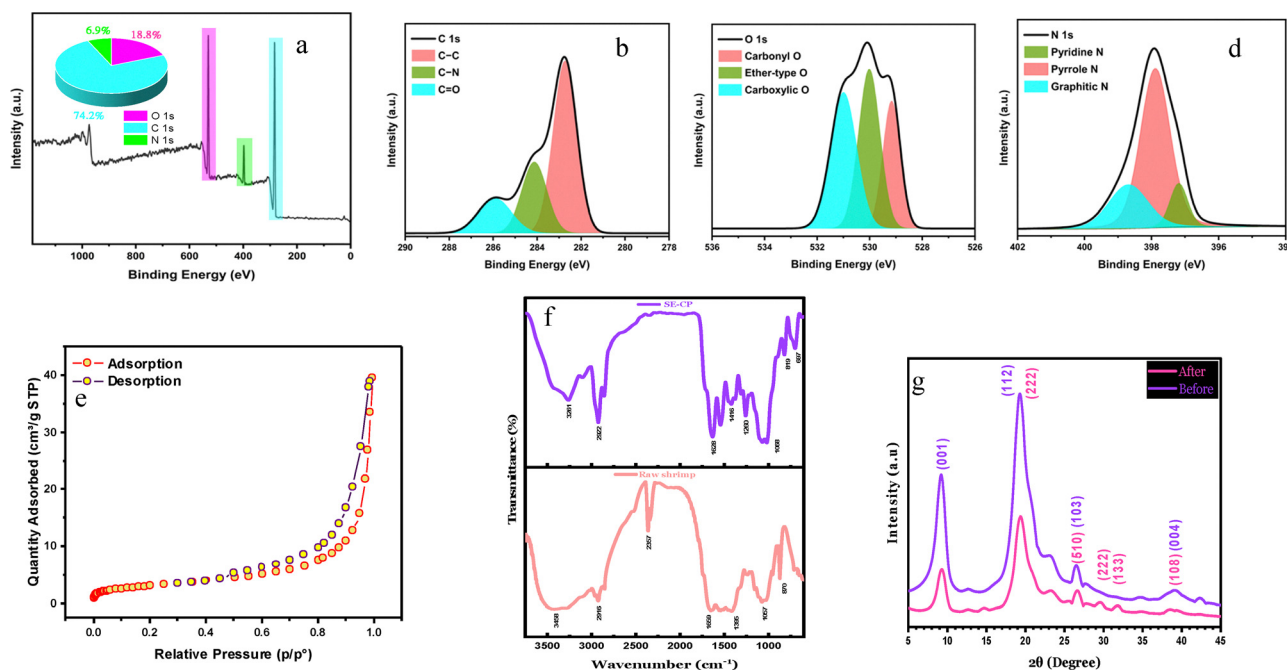
Fig. 1 Different characterization spectra of the SE–CP sorbent: (a) wide scan XPS spectrum of SE-CP; (b) C 1s high resolution deconvoluted XPS; (c) O 1s high resolution deconvoluted XPS; and (d) N 1s high resolution deconvoluted XPS; (e) nitrogen sorption and desorption isotherms; (f) FTIR spectra; (g) XRD spectra.

shown in Fig. 1(e). These data have also been analyzed using the BET method to obtain the surface area and total pore volume of the sample. The BET surface area (S_{BET}) of SE-CP was 51.4914 m^2 g^{-1} and the total pore volume of the biosorbent was 0.135293 cm^3 g^{-1}. The correlation of these data indicates a highly porous solid with numerous mesoporous pores and average specific surface areas.[25] This indicates the possibility of a multilayer biosorbent, which will be confirmed using other characterization studies, with a low specific surface area and a highly porous structure.[26] Nevertheless, during the biosorption process, in addition to the meso-pores, numerous active sites will be available to interact with the pollutants.

3.1.3. Functional surface groups of the SE-CP biosorbent as determined by the FTIR method. The FTIR spectra of the raw shrimp exoskeletons compared with those of the prepared SE-CP biosorbent (Fig. 1(f)) show broadly similar bands. The band at 3261 cm^{-1} is attributed to hydroxyl (OH) and amine (NH) groups and also to hydrogen bonding.[27] In view of the different stretching vibration bands, the bands occurring in the range of 3425–2881 cm^{-1} are assigned to the association of N–H and NH$_2$ groups in primary amines.[28] Additionally, stretching vibrations occurring in the range of 2922–2879 cm^{-1} correspond to the methyl group in NHCOCH$_3$, the methylene group in CH$_2$OH and the methyl group in the pyranose ring of chitin.[28,29] Accordingly, the band around 1650 cm^{-1} corresponds to the axial stretching of C=O bonds in chitin/chitosan amide I and amide II. This band around 1650 cm^{-1} was expected due to the presence of chitin oligonucleotides in the extracted powder. However, the ethylene group cleavage band was also observed at 1416 cm^{-1}. Similarly, the absorption bands around 1068 cm^{-1} and 891 cm^{-1} confirm the binding of monomers by β-glycosidic bonds.[30] The SE-CP spectrum showed the appearance of a new peak at 1260 cm^{-1} corresponding to α-chitin, which confirms the presence of α-chitin–protein nanofibers in the SE-CP powder.

3.1.4. Assessment of the α-chitin crystallinity by the XRD method. The SE-CP and the SE-CP@SB XRD diffractograms, respectively, before and after SB biosorption, are shown in Fig. 1(g). Three similar peaks can be observed at $2\theta = 9.3°$, 19.5° and 26.9°, showing the presence of α-chitin in the SE-CP and the SE-CP@SB samples. Furthermore, the absence of the calcite peak proves that the mineral layer has been successfully removed from the raw shrimp exoskeleton. Typically, four peaks characterize the crystalline reflections of α-chitin at $2\theta = 9.3°$, 12.6°, 19.1°, and 26.2°. Our XRD data for the α-chitin are in good agreement with those reported in the literature, indicating that α-chitin has a degree of crystallinity comparable to the coherent peaks already found.[31,32] In addition, Fig. 1(g) shows weak peaks at $2\theta \geq 35°$, which are generally secondary to dye biosorption. It should be noted that the occurrence of α-chitin remained significant in the spectrum even after the biosorption process.

3.1.5. Texture of the SE-CP surface as obtained by SEM analysis. The SEM images of the SE-CP surface show that the surface resulting from demineralization is heterogeneous, with parts presenting several micropores, leading, hence, to a favorable environment for the biosorption process (Fig. 2(a) and (b)). The acid treatment has increased the porosity of the material, which is no longer smooth as reported in the literature[9,33] (Fig. 2(c) and (d)). The chemical analyses of three points (spots) of the same surface were assessed by the XDE measurements as depicted in Fig. 2(e), (g) and (i). Overall, the analysis was broadly similar between the three analyses carried out, with the strong presence of C, O and N signals in all three spectra proving the presence of α-chito-protein (C–O–NH complex). However, small amounts of Cl, S and P are also present, perhaps due to the marine origin of the biomaterial. Furthermore, adhesion onto the surface of the dye particles is evident, which is illustrated by SE-CP@SB images, also revealing the presence of macroscopic holes and facilitating, hence, the pollutant biosorption process. For additional information concerning the nature of the adsorbed particles, elemental analyses were carried out to study in greater detail the particles detected by the SEM images. These findings show that the particles adsorbed onto the surface belong to a complex chemical molecule, the ''dye''. This particle contains mainly O, followed by C and N, with the addition of various quantities of the elements Si, Fe, Mg, Al, and Ca. These results confirm the retention of the SB dye onto/by SE-CP. Surface analysis also reveals elements similar to those previously shown by SE-CP, with the exception of the presence of Na. This element is already present in the raw material (shrimp exoskeleton) due to its marine nature.[34,35] After analysis of the surface hole, the elements detected in Fig. 4(a), which represents the adsorbed dye, are present in large amounts, demonstrating the proper uptake of the SB dye by the SE-CP biosorbent. Consequently, SE-CP can adsorb (on the surface) and absorb (through the pore) contaminants at the same time.

3.1.6. SE-CP particle shape and size as obtained by TEM analyses. TEM analyses were carried out to determine the particle shape and size of the SE-CP biosorbent. TEM images of the SE-CP particle at different magnifications are shown in the SI. As can be seen in this figure, a large number of particles agglomerate at 100 nm and above, representing a macro-hierarchical nanofiber structure of the chito-protein complex. In particular, at 50 nm, numerous chitin-bound protein sheets become visible, giving the material a nano-porous appearance. Thus, the transformation of the biomaterial into a nano-porous state, with pore sizes smaller than 100 nm, is observed.[36] The high porosity of SE-CP opens up the possibility of increasing its efficiency as a biosorbent, even with a moderate specific surface area (Fig. 1(e)).

3.1.7. Variation of the surface charge of the SE-CP biosorbent in the presence of a dye. The streaming induced potential (SIP) variation of the SE-CP biosorbent as a function of the added amount of dye (SB and SR) are shown in the SI. As can be observed in this figure, the normalized SIP value (ratio of the actual SIP value to its absolute maximum value at the highest added dye volume) decreases from 0.4 and reaches the value of 0, after the addition of 1.6×10^{-8} and 3.5×10^{-8} moles of SB and SR dyes, respectively. These decreases in the biosorbent SIP value and its surface charge neutralization are due to the
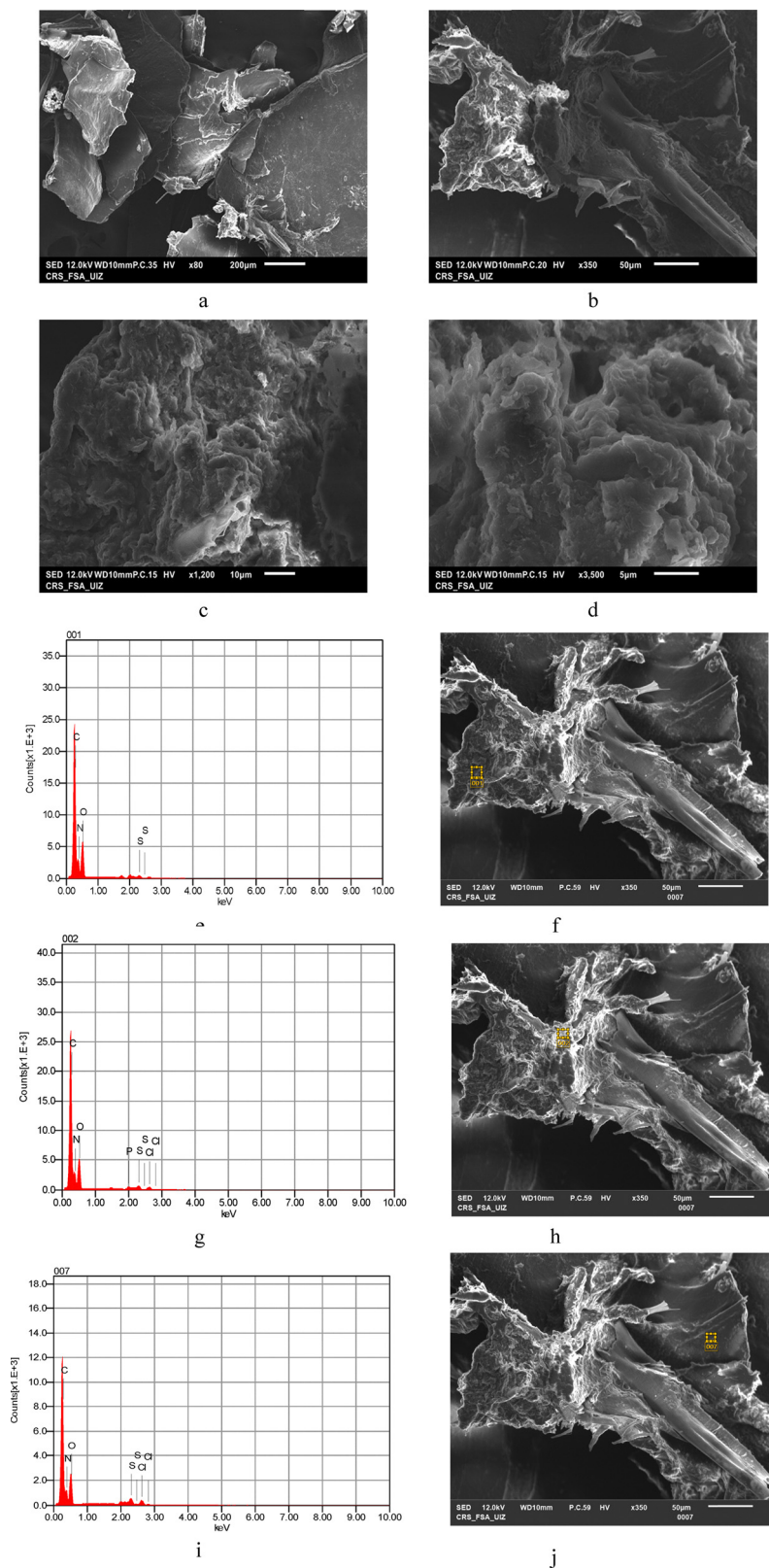
Fig. 2 SEM images of SE-CP at different magnifications: (a) 200 μm, (b) 50 μm, (c) 10 μm and (d) 5 μm and EDX spectra of the SE-CP biomaterial from an acid-etched section (e), (g) and (i) and corresponding SEM images (f), (h) and (j).

electrostatic interaction occurring between the positively charged α-chito-protein complex and the anionic dyes. Hence, the SB dye saturates the positively charged biosorbent surface with less amount in comparison to the SR dye, which is due to the biosorbent efficiency in rapidly sticking negatively charged molecules to its positive sites. The overall data indicate that the SE-CP biosorbent contains more positive charges (amine group) than negative charges on its surface. The dye biosorption transforms the SE-CP from a positively to negatively charged surface, resulting from the presence of nano-porous on the biosorbent surface, which will be validated later in the isotherm study.

3.1.8. Particle size of the SE-CP biosorbent. The particle size was also measured by DLS. The SE-CP biosorbent exhibited an average particle size of 1253.3 nm in an acidic medium with pH = 2. Clearly, the particle size of a biopolymer is larger than that of a single dye molecule. In this respect, the three recorded values of 1210 nm, 1170 nm and 1380 nm demonstrate the uniformity of particle dispersion in the liquid. These particles take the form of the main macro-hierarchical α-chito-protein complex. On the whole, longer chitin fibers exhibit better performance compared to this biocomplex; the stiffness, strength and ductility of the α-chito-protein complex are optimized when the incorporated chitin fibers are longer than 20 nm.[37] Thus, the particle measured can be a set of well-stacked fibers. As the complex represents the zigzag structure between adjacent chitin layers, it takes on the shape of a saw tooth.[37,38] Nevertheless, this aspect becomes more evident when the length of the chitin fibers exceeds 15 nm.[37] At this point, the structure of the fibers making up the particle is saw tooth-shaped. Furthermore, the deformation of the spacing

between the α-chito-protein complex decreases as the length of the chitin fibers increases, suggesting a healthy spacing between the chitin-protein complex which will enable efficient biosorption.

3.2. Batch biosorption studies of SB and SR dyes on the SE-CP surface

3.2.1. pH effect. The influence of pH on the biosorption of SR and SB ions by SE-CP was analyzed in order to assess the optimum pH necessary to accomplish the treatment (Fig. 3(a)). Note that the pH of the solution regulates the surface charge of SE-CP, as well as the charge of the metal ions present in the solution. To this end, pH-dependent dye biosorption studies were carried out at room temperature using 0.05 g of the biosorbent and a dye solution with a concentration of 75 mg L^{-1}, during a contact time of three hours, and at a stirring speed of 100 rpm. The results shown in Fig. 3(a) clearly indicate that the biosorption efficiency decreases with increasing pH, particularly in the basic range, with the possible persistence of the "buffer effect" that has stabilized the SR curve. This is a common phenomenon when it comes to biobased materials due to their complexity.[39] In order to enable biosorption of the dye by SE-CP, the optimum pH values for the SR dye were found to be set at pH = 3 and pH = 4 for the SB dye. With increasing pH, the ions of both dyes were mainly available in negative forms and they required more positive surface charges for biosorption. Similarly, the positive surface charge of the biomaterial studied was reduced with increasing pH due to the less availability of the H$^+$ ions in solution, resulting in a decrease in biosorption efficiency. A low pH was found to be more suitable for biosorption of both dyes by using the SE-CP
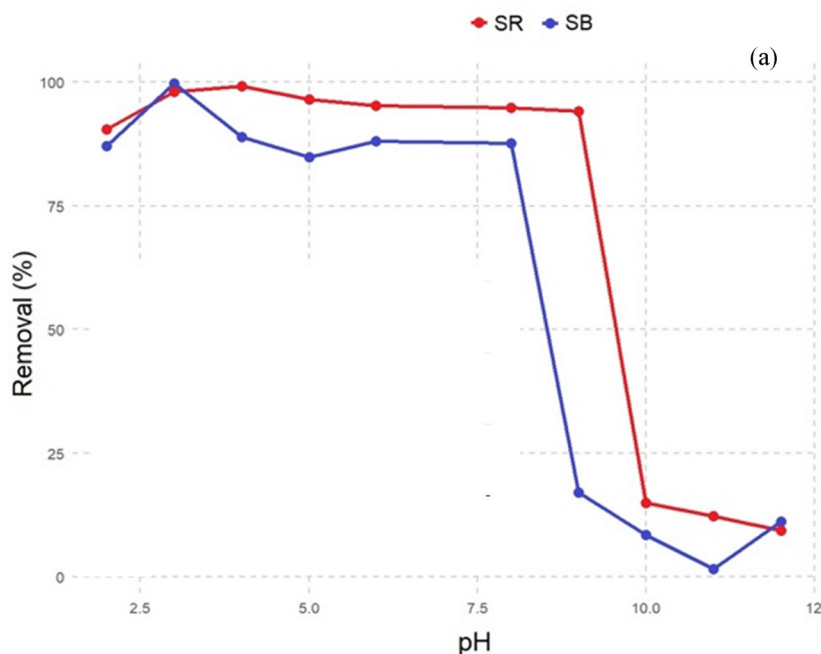

Fig. 3 (a) Effect of pH on the removal efficiency of the two treated dyes at a concentration of 75 mg L^{-1} by 0.05 g of SE–CP and (b) point of zero charge (PZC) of the SE–CP biomaterial.

biosorbent. Thus, lowering the aqueous phase pH may affect the surface properties of the biosorbent. It should be noted that α-chito-protein acts as a polyelectrolyte whose overall charge depends on the pH of the aqueous medium.[40]

3.2.2. PZC of the SE-CP biosorbent. The pH at which the net positive charge of the side chains is balanced by the net negative charge is called the point of zero charge (PZC), and the macromolecule is electrically neutral. The measured PZC value of the SE-CP was used to explain the electrostatic interactions involved in the solution (Fig. 3(b)). The initial pH of the solution ($pH_{solution}$) strongly affects the biosorbent surface charges, the degree of ionization and the pollutant solubility. When $pH_{solution} = pH_{PZC}$, the biosorbent surface becomes neutral. When $pH_{solution} < pH_{PZC}$ of the biosorbents, the surface charge of the biosorbents is positive due to protonation of the surface functional groups.[41,42] Consequently, the pH variation alters the electrostatic interactions occurring between the adsorbent and the pollutant due to opposite surface charges. Hence, at $pH_{solution} > pH_{PZC}$, the macromolecule carries a net negative charge, given by the deprotonated carboxyl groups ($-COO^-$). At pH = 3 for SR and pH = 4 for SB, the number of positively charged active sites capable of interacting with dye anions increases significantly, leading to the increase of the retention capacity of chitin and proteins. A good correlation was observed between the isoelectric point measured by the pH variation of the SE-CP biosorbent and the PZC determined by the SIP measurement upon the SE-CP titration by using both dyes. Maximum elimination was recorded for the SB and SR dyes at pH < PZC, confirming that the polymer carries a net positive charge, given by the protonated amine groups of the side chains ($-NH_3^+$). Thus, at pH = 3 and pH = 4, some of the SE-CP surface functional groups present due to chitin (e.g. –OH and –CO) were protonated and they become positively charged.

3.2.3. Dose effect. Batch biosorption experiments were also carried out by varying the amount of SE-CP from 0.02 to 0.2 g in order to examine the effect of SE-CP dose on both dyes' removal, under the following experimental conditions: pH = 4 for SR and pH = 3 for SB, a stirring speed of 100 rpm, a contact time of three hours, room temperature, and an initial feed concentration of 75 mg L^{-1}. Maximum biosorption efficiencies of almost 100% were recorded at biosorbent masses of 0.04 g L^{-1} and 0.08 g L^{-1}, for SB and for SR, respectively (Fig. 4). Hence, at the lowest biosorbent mass of 0.02 g, the abatement reached values over 97% for both dyes studied. Increasing the number of active sites improved dye biosorption at low biosorbent dosages (up to 0.04 g L^{-1} for SB and up to 0.08 g L^{-1} for SR). The decrease in biosorption efficiencies for higher biosorbent dosage values (above 0.14 g L^{-1} for SB and above 0.16 g L^{-1} for SR) is probably due to overlapping, aggregation and stacking effects of the biosorbent due to their higher concentration values.[43,44] Therefore, the optimal biosorbent dosage level was used for further experimental investigations. In this context, the presence of chitin and proteins leads to an efficient biosorbent mainly at low dosage and at acidic pH. In the following, in order to investigate other parameters affecting the dye removal, only the optimal conditions were considered.

3.2.4. Contact time effect. The dye removal performance by the biosorbent as a function of the contact time and the initial feed concentration were examined by carrying out biosorption studies under the optimum conditions for each dye (SR and SB). Hence, the contact time varied from 0 to 250 min, whereas the initial feed concentration for both dyes was fixed at
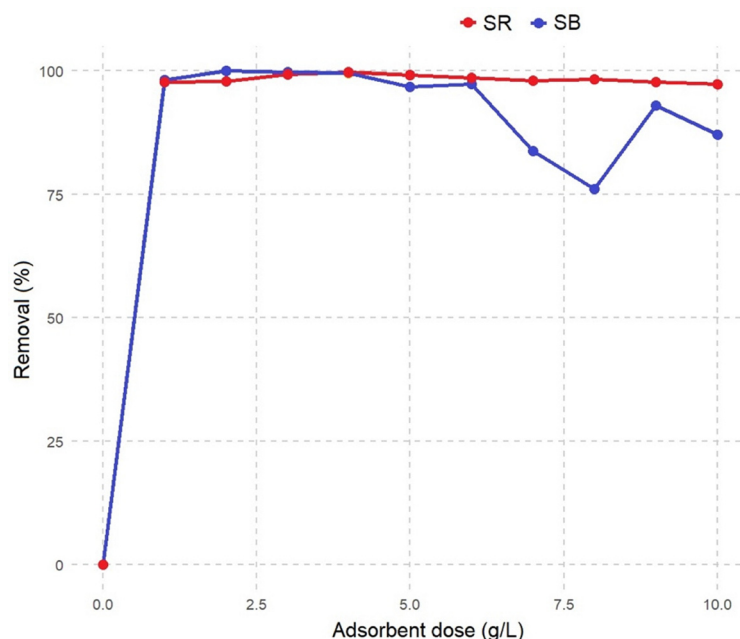

Fig. 4 (a) Effect of SE-CP biosorbent dose/dosage on the removal efficiency of two dyes studied at an initial dye concentration of 75 mg L^{-1} and pH = 4 for SR and pH = 3 for SB.
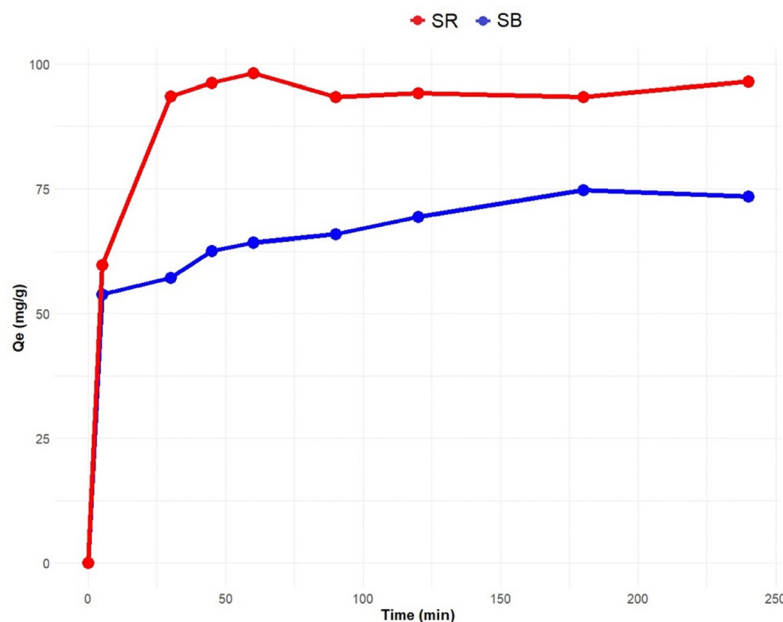
Fig. 5 Effect of the contact time on biosorption performance of the SE–CP biomaterial at a concentration of 75 mg L^{-1} and pH = 4 for SR and pH = 3 for SB at room temperature.

75 mg L^{-1}. As shown in Fig. 5, the biosorption capacity of the SE-CP material showed a rapid increase over the first 5 min, after which it levels at 100 min. At the beginning and due to the excessive availability of biosorbent surface active sites for the attachment of negative ions, there was an initial rapid increase in the biosorption capacity of the SE-CP after only 100 minutes. Thereafter, the biosorbent active sites were saturated, resulting in a small increase in SE-CP removal capacity.[45] Therefore, a contact time of 100 minutes was subsequently determined to be the optimum biosorption time for the ionic binding of the two anionic dyes to the SE-CP biomaterial surface.

3.2.5. Initial feed concentration effect. It is apparent in Fig. 6, showing the effect of the initial feed concentration on biosorption performance of SE-CP, that in the dye concentration range of 50 to 300 mg L^{-1}, an abatement rate of over 80% is recorded for the SR and SB dyes. The concentration gradient leading to the biosorption process widened considerably with the higher dye initial concentration (up to 300 mg L^{-1}), improving biosorptive capacity values for the SE-CP biomaterial. However, the removal efficiency of the two acid dyes by the biosorbent decreased slightly at the highest initial feed concentration (300 mg L^{-1}), where an increase in the competition between ions for biosorption occurs on the limited active sites of SE-CP, leading to a slight decrease in removal efficiency.[46,47] Therefore, the abatement rate for a dye concentration of 75 mg L^{-1}, for SB and SR dyes, was the best (close to 100% in previous tests), and this dye concentration will be considered as an optimal value.

3.2.6. Temperature effect. Initial pollutant concentrations have a major influence on sorption capacity. The effects of the initial concentration of the two dyes SR and SB on the biosorption performance of SE-CP at different temperatures (20, 30, 40 and 50 °C) are examined. A good removal rate of 80–100% is reported for 50 to 300 mg L^{-1} for both dyes SB and SR. Such removal is not overly influenced by the temperature changes in the SR dye concentration range investigated. However, after a dye concentration of 200 mg L^{-1}, for all temperatures studied, a slight decrease in biosorption of the SR dye by SE-CP is noted. When the dye concentration increases, an increased competition between ions for biosorption occurs as well, on the limited active sites of SE-CP, leading to a slight decrease in the removal efficiency.[48,49] The most effective reduction occurs at a temperature of 40 °C for all concentrations. The temperatures of 30 °C and 20 °C show a slightly lower reduction rate than that recorded at 40 °C. At 20 °C, and at a concentration above 100 mg L^{-1}, biosorption decreases with increasing SB dye concentration. Compared with the SB dye, SE-CP achieves a dye removal efficiency of almost 99% at low initial dye concentrations ($<$100 mg L^{-1}), due to the high availability of empty binding sites.[50,51] In contrast, high initial dye concentrations tend to leave most adsorption sites occupied by dye molecules, while others remain in solution, slightly reducing removal efficiency. As a result, even room temperature (around 20 °C) can be effective for biosorption of the SR dye at a concentration below 200 mg L^{-1} and the SB dye at a concentration below 100 mg L^{-1}. This difference can be justified by the interaction of dye molecules with the macro-hierarchical complex of chito-protein which is not affected by the temperature. For this reason, an ambient temperature will be recommended to complete the biosorption study of the SE-CP biosorbent, since the optimal concentration chosen is 75 mg L^{-1} for the two dyes studied.

3.3. Biosorption kinetics

Kinetic analysis of the interactions occurring between red acid and SE-CP is crucial for the design and scale-up studies of the biosorption process.[52] Thus, experimental data were compared
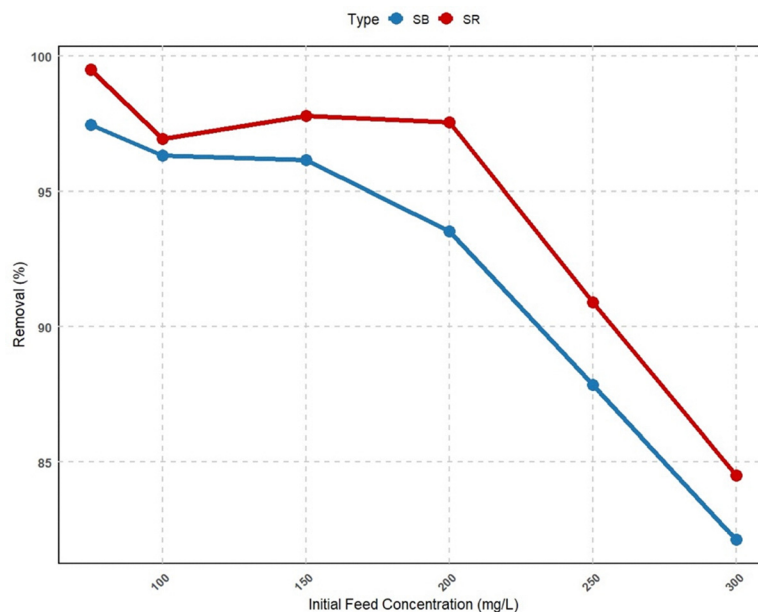
Fig. 6 Effect of the initial dye concentration on biosorption performance of the SE-CP biomaterial at pH = 4 for SR and pH = 3 for SB at room temperature SE-CP dosage.

to three kinetic theoretical models such as the pseudo-first-order, pseudo-second-order and intra-particle diffusion models. Modeling was carried out for experimental biosorption results obtained at pH = 3 for SR and pH = 4 for SB, a stirring speed of 100 rpm, a temperature of 20 °C, a dye concentration of 75 mg L^{-1}, and a biosorbent dosage of 0.08 g for SR and 0.04 g for SB. The results clearly show that the dye biosorption onto the material surface obeys a pseudo-second-order kinetic model. In fact, the correlation coefficients of this model with the experimental data showed the highest R^2 value, equal to 0.998 for the optimal feed concentration of 75 mg L^{-1}, as compared with the pseudo-first-order model. However, it was reported elsewhere[50] that the experimental biosorption data fitted with the pseudo-first-order model and demonstrated that electron transfer mechanisms were involved in dye binding onto the biomaterial surface.[53] The pseudo-second-order kinetic theoretical model as determined for the red acid biosorption onto the biomaterial surface implies a rapid initial rate of biosorption followed by a slower secondary step to reach equilibrium. The characteristics of the pseudo-second-order model are in agreement with the experimental results, as shown in the SI. Finally, the intraparticle diffusion model was also tested to verify the possible influence of mass transfer resistance on SR dye binding to SE-CP. Overall, the tests showed an R^2 of 0.961, underlining that this model can also be applied to describe the adsorption kinetics of the SR dye. Kinetic constants were obtained by non-linear regression. As for the removal of the SR dye and based on the correlation coefficients calculated, the pseudo-second-order model was found to be the best suited to explain the adsorption kinetics of blue acid on the material with the R^2 value equal to 0.998. Moreover, the intra-particle diffusion model was also tested with an R^2 of 0.961. Consequently, the experimental adsorption capacity of

SB was very close to the values calculated by the pseudo-secondary order model. The kinetic study showed that the adsorption process occurs in 2 steps. The first one takes few minutes, during which 80% of the equilibrium adsorbed quantity is achieved, whereas in the second step taking several hours of contact, the adsorbed amount remains constant.

3.4. Equilibrium biosorption isotherm models

It should be noted that the adsorption models are best determined by non-linear regression analyses, which represent mathematically rigorous methods for determining the adsorption model parameters using equations in their original forms. Hence, the non-linear Langmuir, Freundlich and Elovich models were used in this work to investigate the biosorption equilibrium of the two acid dyes on the material studied (Fig. 7). The overall data indicate a heterogeneous distribution of the material surface active sites, with Freundlich's model being the best for describing adsorption consisting of multi-layers when SR is adsorbed onto the SE-CP surface with an R^2 of 0.966 (Table 2). On the other hand, in the case of SB on SE-CP, the three models studied Langmuir, Freundlich and Elovich showed R^2 values close to 0.858, 0.781 and 0.978, respectively. The reason may lie in the adsorption of the dyes on separate monolayers, and as the best-fitting model is the Freundlich model, the monolayer surface is heterogeneous. In addition, the nature of the adsorption process was investigated by calculating the values of the Freundlich constant '$1/n$'.[54] For both dyes, SR and SB, these were less than 1, and they were 0.37 and 0.60, respectively, confirming that biosorption is favorable on SE-CP. Indeed, Freundlich constant values ranging from 0.1 to 0.6 demonstrate the high adsorption capacity. This phenomenon is also attributable to the Langmuir isotherm, since the R_L is an important parameter for evaluating the affinity of the
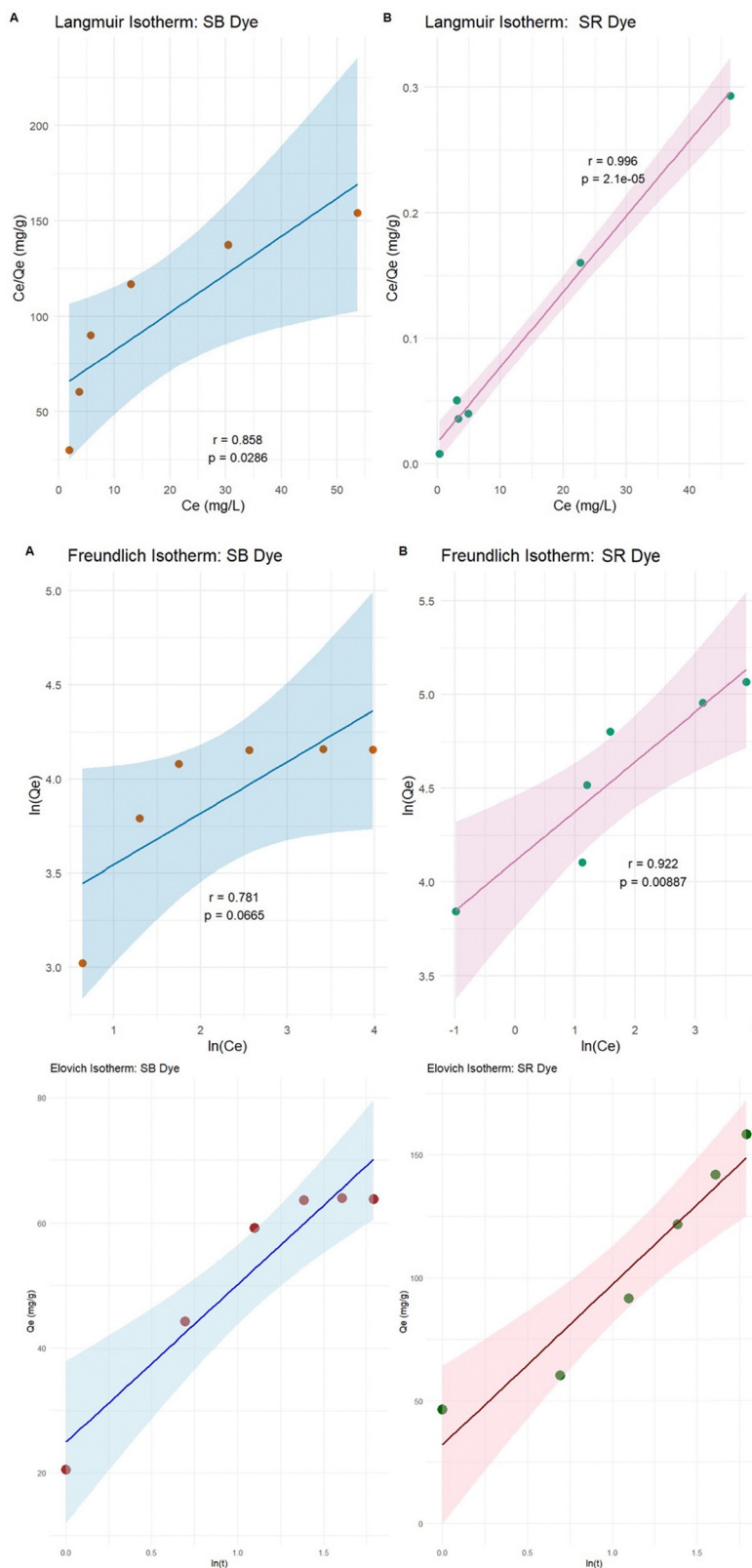
Fig. 7 Study of the biosorption isotherms of red and blue acid dyes on SE-CP at room temperature.

binding sites. Setting the R_L between 0 and 1 indicates "favorable adsorption" of the dye onto the adsorbent.[54] The maximum adsorption quantity Q_{max} of SB (up to 63.81 mg g^{-1}) is well below that of SR (up to 158.43 mg g^{-1}). Note that the adsorbed quantities during a contact time of 250 minutes, q_t, were 45.27 mg g^{-1} for SR and 34.45 mg g^{-1} for SB. In

Table 2 Freundlich, Langmuir and Elovich constants for adsorption of SB and SR onto SE-CP

Langmuir

	Q_m (mg g^{-1})	K_L (L mg^{-1})	R^2
SB	63.815	1.370	0.858
SR	158.432	0.811	0.996

Freundlich

	K_F (mg^{1-n} L^n g^{-1})	$1/n$	R^2
SB	16.859	0.607	0.781
SR	43.860	0.373	0.922

Elovich

	α (mg g min^{-1})	β (g mg^{-1})	R^2
SB	83.205	0.084	0.978
SR	68.771	0.612	0.843

comparison with other studies using activated carbon,[55–58] the maximum biosorption capacity exhibited by SE-CP in the present study is highly attractive and can even rival those obtained with activated carbon. Indeed, the multilayer biosorption of the biomaterial studied enables it to trap a wide range of pollutants. This biomaterial might be used as an alternative, in the near future, to solve the separation problem and could be marketed as a reference adsorbent for the removal of toxic pollutants.

3.5. Thermodynamics of biosorption

Plotting $\ln(K_L)$ as a function of $1/T$ for SR and SB dyes produces two straight lines (Fig. 8). Normally, the adsorption capacity increases when the temperature increases. However, in the case of SR, adsorption capacity was found to decrease with increasing temperature. This scenario can be attributed to the fact that as temperature increases, the energy supplied to SR ions to achieve the required activation energy exceeds the desired amount and causes a reverse in the diffusion effect towards the adsorbent active sites available for binding. The associated thermodynamic parameters were also calculated and are presented in Table 3. Negative ΔG values indicate the spontaneous nature of the adsorption process at 20, 30, 40 and 50 °C. If ΔG is negative and ΔH is positive at one temperature, the adsorption process is a spontaneous endothermic reaction and, furthermore, the more negative ΔG is, the more readily the dye is adsorbed by the material. Moreover, $\Delta S > 0$ indicates an increase in the degree of disorder in the adsorbed layer at the solid/solution interface. Taking into account that the heat of adsorption is the negative enthalpy of adsorption, in the current study, the heat of adsorption of both anionic dyes is then negative and less than 40 kJ mol^{-1}, indicating that the adsorption process is mainly physisorption.

3.6. Reusability and weight stability of SE-CP

The reuse of the biosorbent and the weight stability of the adsorbed material can be achieved by regenerating the
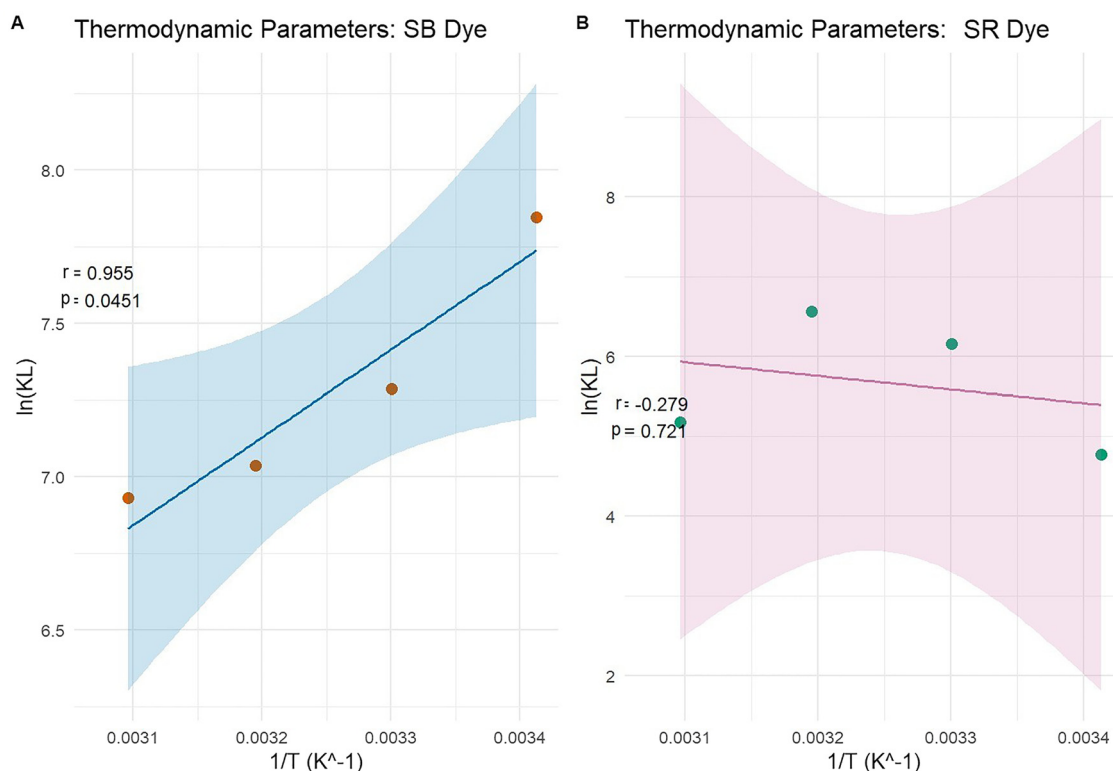
Fig. 8 Adsorption data modeling using the Van't Hoff equation for the two studied dyes.

Table 3 Thermodynamic biosorption parameters of the two dyes studied

Adsorption of Sellacid Red (SR)			
T (°C)	ΔG (kJ mol^{-1})	ΔH (kJ mol^{-1})	ΔS (J k^{-1} mol^{-1})
20	−11.63	68.81	275.67
30	−15.53		
40	−17.09		
50	−13.91		
Adsorption of Sellaset Blue (SB)			
20	−19.11	23.84	17.04
30	−18.36		
40	−18.31		
50	−18.61		

dye-loaded SE-CP. Regeneration of the biomaterial after biosorption is illustrated in the SI, using two solvents: distilled water (DW) and sodium hydroxide (NaOH) for both dyes SR in SR@DW/SR@NaOH and SB in SB@DW/SB@NaOH. After each SE-CP regeneration cycle, weight recovery is illustrated in the SI. Several aspects were monitored during the regeneration process to ensure ease of reuse while minimizing costs. Upon the fifth regeneration cycle with DW, the SB@DW dye exhibited a removal rate higher than that registered for the SR@DW dye, with respective abatement rates of 76.82% and 67.27%. Moreover, the dyes can be desorbed using green solvent such as DW, minimizing regeneration loads, with a significant reduction up to the fifth regeneration cycle, demonstrating the added value of using SE-CP as a biomaterial. After each regeneration cycle, the recovered mass appears to decrease for both dyes, demonstrating the presence of a biosorption phenomenon that generates a loss of mass with each cycle. At the fifth cycle, SB@DW and SR@DW dyes show mass recovery percentages of 77.17% and 62.58%, respectively. This represents good mass recovery after biosorption, confirming that SE-CP is effective in terms of dye removal, even after desorption by DW only. The application of NaOH for SE-CP desorption after biosorption of SR@NaOH and SB@NaOH showed similar efficiencies. Biosorption removal rates reached 83.53% and 82.14% for the fifth regeneration cycle of the SB@NaOH and SR@NaOH dyes, respectively. However, the mass recovered by NaOH is lower than that recovered by DW. Meanwhile, a mass recovery percentage of 33.33% is recorded for the SB dye, while for SR, 59.17% is obtained. This decrease may be due to the sensitivity of the chito-protein complex to alkaline solution (deproteinization process). Finally, the SE-CP seems to be a promising biosorbent and can be considered sustainable, if DW is used as solvent for desorption, due to the low mass loss, which is not very significant.

3.7. SEM/EDX analyses of the reusable SE-CP

After five NaOH regeneration cycles, the SE-CP was assumed to be reusable for SR@NaOH dye biosorption (SI). To confirm this hypothesis, we carried out an XDE analysis of the particle, which adheres onto the surface of the material (SI) in comparison with the material surface (SI). The analysis regarding the particle shows a strong contribution of the C and O elements,

with traces of Na, Ca and Cu. These elements may be generated after successive interactions with the same material to biosorb the same dye. Furthermore, a section of the same surface shows that the amount of oxygen is greater than that of carbon, with sodium, and traces of Cl and Cu. This is perhaps due to the surface heterogeneity already mentioned (SEM/XDE analysis of SE-CP), where the difference between the amount of carbon and oxygen can be explained by the heterogeneous distribution of active sites on the material surface, resulting in different contents of the particles that make up the pollutant on the material surface. The clear laminate is attributed to the chito-protein complex structure and the NaOH treatment, which partially removes biomaterial proteins with successive treatments. These features can be exploited to extend the biosorption cycles of the SE-CP biomaterial.

The results of SB@NaOH regeneration cycles by using the same SE-CP biomaterial are shown in the SI. The coarse surface of a well-porous biomaterial is clear even after several regenerations. However, dye particles are trapped in these pores due to the non-detection of particles on the surface. Closer magnification revealed the layered nature of the SE-CP even after five regeneration cycles (Fig. 9). In addition, XDE analysis (SI) indicates the dominance of carbon and oxygen at the surface, which are the most important particles on the material surface for both the SE-CP (according to SEM/XDE analysis of the SE-CP) and the dye (azo). Evidence of the elements Ca and Cl is visible, proving that biosorption is deeper than the SEM
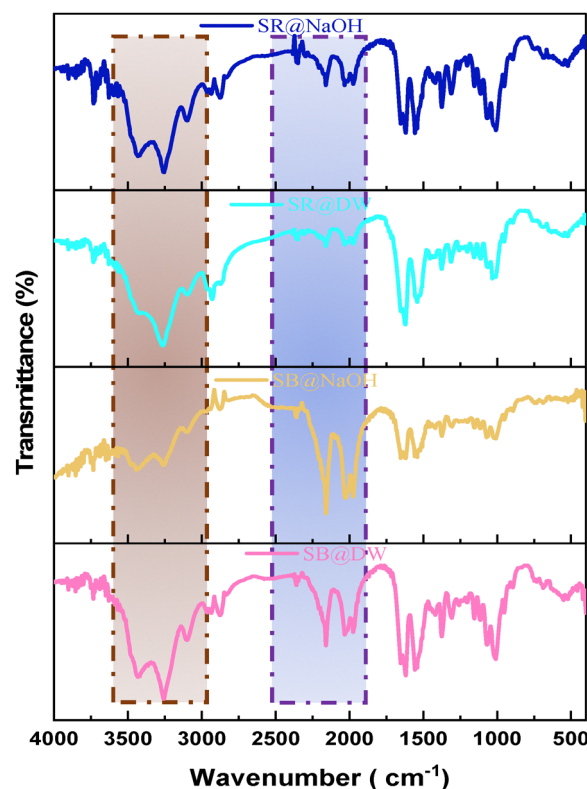

Fig. 9 FTIR spectra of the biosorbent after 5 regeneration cycles by NaOH and DW for each dye.

detector was able to record, given that biosorption occurs in separate monolayers (isotherm applied).

3.8. Biosorption mechanism

The biosorption of SR and SB dyes onto the SE-CP biomaterial is governed by a combination of physicochemical interactions involving the material's structural components, surface functionality, and the electrostatic nature of the dyes. The characterization of SE-CP revealed the coexistence of chitin and proteins, mainly composed of α-chitin (D-glucosamine units), whose antiparallel molecular arrangement confers high crystallinity and chemical stability.[59] The biomaterial surface exhibits abundant hydroxyl, carboxyl, and amino functional groups originating from the chitin–protein matrix, which serve as active sites for dye attachment. The least hydrated and most polarized dye ions are the most strongly adsorbed.

Simultaneously, FTIR, SEM and EDX analyses were carried out to further explore the mechanisms of SB and SR biosorption by the SE-CP bio-element. EDX spectra show the adhesion of particles belonging to the SB dye onto the surface, as well as charged macroscopic holes. These results could lead to the involvement of pore filling, which was confirmed by EDX spectra after five regenerations. In the FTIR spectra, the stretching vibration band of (νO–H) and (νN–H) after biosorption of the anionic dyes shifted separately to 3431.5 cm^{-1} and 3256.2 cm^{-1}, respectively. These results confirm the presence of various functional groups such as –OH, –COOH, and R-OH

on the SE-CP surface, leading to the presence of hydrogen bonding between the SE-CP and the dye molecules.[60] The amide I and amide II peaks also shifted to lower wavelengths, while the peak at 1619 cm^{-1} (νC–N) and the appearance of a new peak at 1009.7 cm^{-1} were attributed to primary amine stretching that could be attributed to π–π interactions. All these changes reflect the involvement of these functional groups in the biosorption process.[61] The structures of both SR and SB dyes contain –SO$_3^-$ groups, which promote electrostatic interactions with the protonated amino groups of chitin at low pH. Under acidic conditions, these –NH$_2$ groups become positively charged (–NH$_3^+$), enhancing attraction to the negatively charged dye ions. Consequently, dye uptake by SE-CP increases as pH decreases, confirming that electrostatic interactions play a dominant role in the biosorption process. Furthermore, in accordance with the XPS results, the presence of pyridinic and pyrrolic nitrogen elements was instrumental in enhancing the nanoporosity of SE-CP, thus increasing the number of active sites. In terms of comparison, many studies[34,62] have focused on activated carbon derived from shrimp shells for its effectiveness, which undergoes pyrolysis, whereas SE-CP is acid-treated and dried at 220 °C without complete carbonization, making it a promising biomaterial. This difference is likely to influence the carbon's spectral characteristics. Meanwhile, being the origin of pyridinic and pyrrolic nitrogen, these functional groups arise due to the reaction of amino and hydroxyl groups during the demineralization process, which
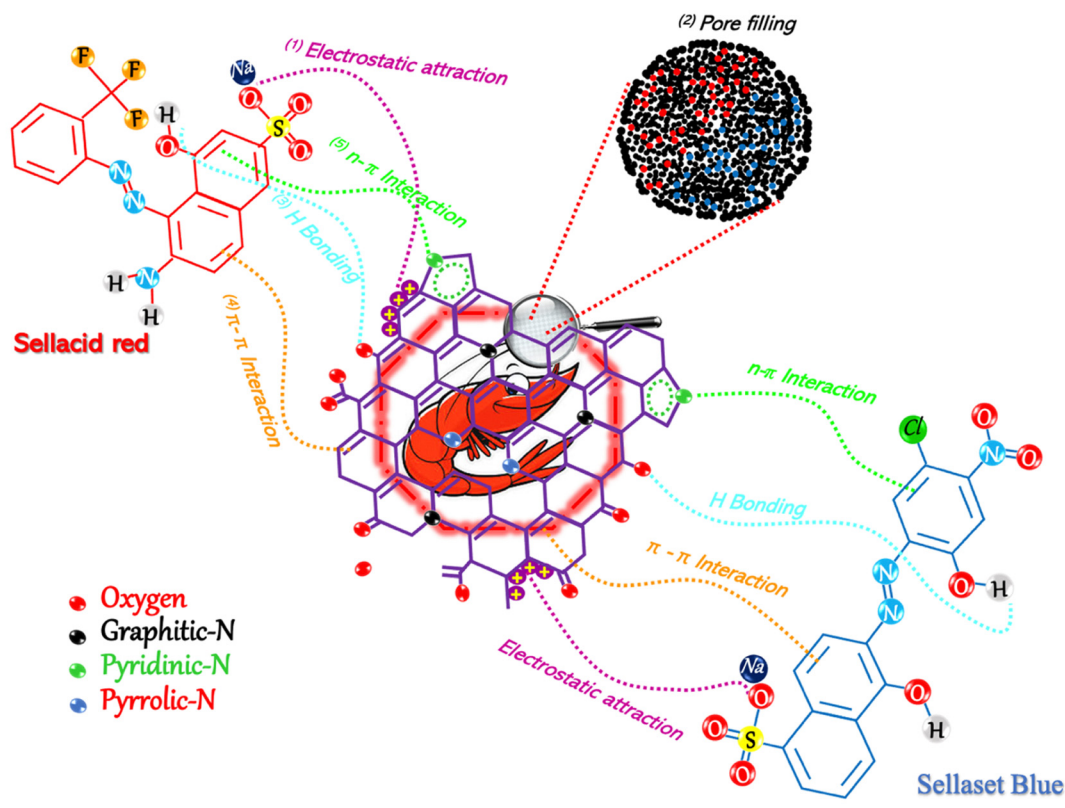

Fig. 10 Graphical depiction of the suggested biosorption mechanism during the biosorption process of SR and SB dyes.

removes the mineral matrix from the shrimp exoskeleton. The observed nitrogen configurations do not necessarily indicate char formation but rather reflect the chemical interactions between chitin-derived functional groups. However, the surface nitrogen species identified by XPS play a crucial role in enhancing the porosity and reactivity of SE-CP. The presence of pyridinic and pyrrolic nitrogen, along with oxygen-containing groups, introduces additional active sites, thereby improving sorption efficiency. These results agree with previous reports showing that graphitic-N improves biosorbent stability and adsorption efficiency. The FTIR spectra further confirm oxygen-containing groups from polysaccharides and proteins that facilitate n–π and electrostatic interactions with anionic dyes. Even after several regeneration cycles (Fig. 10), SE-CP retains its porous structure and remains more effective in removing low-molecular-weight dyes than high-molecular-weight ones.

4. Study limitations

Despite the promising performance of SE-CP as a biosorbent, several limitations should be noted. First, the current study was conducted under batch laboratory conditions, and the effectiveness of SE-CP in continuous-flow or large-scale industrial systems remains to be validated. Second, adsorption experiments were limited to two model anionic dyes (SR and SB); the performance may differ for other dye classes or complex industrial effluents. Third, while SE-CP showed good regeneration over five cycles, long-term stability and potential fouling effects under repeated usage were not fully assessed. Finally, the influence of competing ions or high ionic strength in real wastewater matrices was not evaluated, which could affect adsorption efficiency. Addressing these aspects in future work will be essential to fully demonstrate the practical applicability of SE-CP.

5. Conclusions

In the present work, a modified shrimp exoskeleton (SE-CP) was successfully designed for its use as a biosorbent to remove anionic dyes from aqueous media. The novelty of this new biosorbent is revealed by the function of the chito-protein biocomposite used to remove two anionic dyes from water to reduce liquid and solid (marine by-products) pollution. The SE-CP showed significant removal of the two dyes studied, SR and SB, owing to the heterogeneous distribution of the active sites on the biomaterial surface, leading to multilayer formation. Moreover, the as-prepared biosorbent can be regenerated and reused by using either distilled water or NaOH aqueous solution. Finally, the biosorbent SE-CP offers a high level of efficiency in the removal of dye contaminants from aqueous media, making it a suitable material for sustainable, environmentally friendly remediation.

In future work, the scalability and applicability of SE-CP in continuous treatment systems will be explored to support its integration into industrial wastewater management.

Conflicts of interest

There are no conflicts to declare.

Data availability

All data supporting the findings of this study are available within the article and its supplementary information (SI). Supplementary information is available on request. See DOI: https://doi.org/10.1039/d5ma01010a.

Additional datasets (including raw adsorption data and characterization files) are available from the corresponding author upon reasonable request.

Acknowledgements

References

1 O. C. Basurko, M. Aranda, A. Caballero, M. Andres, J. Murua and G. Gabiña, Workshop on the European Green Deal — Challenges and opportunities for EU fisheries and aquaculture Part I: Decarbonisation & circular economy aspects for fisheries STUDY Requested by the PECH Committee Policy Department for Structural and Cohesion Policies Directorate-General for Internal Policies PE, 2023.

2 N. Nouj, Z. Majbar, M. R. Abelouah, A. Ben Hamou, A. Chaoui, N. Hafid, M. Benafqir, N. El Alem, A. Jada, H. Ouachtak, A. Ait Addi, I. I. Buciscanu, V. Maier, G. Soreanu and I. Cretescu, Eco-friendly wastewater treatment using a crab shell-based liquid bio-coagulant: Multi-criteria decision analysis related to different pollutants separation, *J. Environ. Chem. Eng.*, 2024, **12**(2), 112318, DOI: 10.1016/j.jece.2024.112318.

3 FAO Aquaculture News, FAO, Rome, 2023. https://www.fao.org/publications.

4 M. R. Abelouah, M. Ben-Haddad, S. Hajji, N. Nouj, M. Oueheddou, B. Mghili, G. E. De-la-Torre, L. L. Costa, M. Banni and A. Ait Alla, Exploring marine biofouling on anthropogenic litter in the Atlantic coastline of Morocco, *Mar. Pollut. Bull.*, 2024, **199**, 115938, DOI: 10.1016/j.marpolbul.2023.115938.

5 W. Y. Mo, Y. B. Man and M. H. Wong, Use of food waste, fish waste and food processing waste for China's aquaculture industry: Needs and challenge, *Sci. Total Environ.*, 2018, **613–614**, 635–643, DOI: 10.1016/j.scitotenv.2017.08.321.

6 M. R. Abelouah, M. Idbella, N. Nouj, M. Ben-Haddad, S. Hajji, M. Ouheddou, J. Ourouh, G. Iacomino, R. El Haouti, I. Barra, J. A. Oualid, G. Bonanomi, M. Banni and A. A. Alla, Marine plastic exposure triggers rapid recruitment of plastic-degrading bacteria and accelerates polymer-specific transformations, *J. Hazard. Mater.*, 2025, 137724, DOI: 10.1016/j.jhazmat.2025.137724.

7 S. Hajji, M. Ben-Haddad, M. R. Abelouah, N. Rangel-Buitrago and A. Ait Alla, Microplastic characterization and assessment of removal efficiency in an urban and industrial wastewater treatment plant with submarine emission discharge, *Sci. Total Environ*, 2024, **945**, 174115, DOI: 10.1016/j.scitotenv.2024.174115.

8 I. Ahuja, E. Dauksas, J. F. Remme, R. Richardsen and A. K. Løes, Fish and fish waste-based fertilizers in organic farming – With status in Norway: A review, *Waste Manage.*, 2020, **115**, 95–112, DOI: 10.1016/j.wasman.2020.07.025.

9 N. Nouj, N. Hafid, N. El Alem and I. Cretescu, Novel liquid chitosan-based biocoagulant for treatment optimization of fish processing wastewater from a Moroccan plant, *Materials*, 2021, **14**(23), 7133, DOI: 10.3390/ma14237133.

10 N. Zhou, G. Wei, X. Chen, B. Wu, H. Li, Q. Lu, X. Cao, A. Zhang, K. Chen and P. Ouyang, Self-sufficient biocatalysts constructed using chitin-based microspheres, *Chem. Eng. J.*, 2023, **459**, 141660, DOI: 10.1016/j.cej.2023.141660.

11 N. E. Mushi, T. Nishino, L. A. Berglund and Q. Zhou, Strong and Tough Chitin Film from α-Chitin Nanofibers Prepared by High Pressure Homogenization and Chitosan Addition, *ACS Sustainable Chem. Eng.*, 2019, **7**, 1692–1697, DOI: 10.1021/acssuschemeng.8b05452.

12 C. K. S. Pillai, W. Paul and C. P. Sharma, Chitin and chitosan polymers: Chemistry, solubility and fiber formation, *Prog. Polym. Sci.*, 2009, **34**, 641–678, DOI: 10.1016/j.progpolymsci.2009.04.001.

13 M. Feng, X. Lu, D. Hou and S. Zhang, Solubility, chain characterization, and derivatives of chitin, *Handbook of Chitin and Chitosan: Preparation and Properties*, Elsevier, 2020, vol. 1, pp. 101–129, DOI: 10.1016/B978-0-12-817970-3.00004-3.

14 S. Shukla, A. Sharma, G. Rathi, A. Manchanda, A. Khan, M. A. Malik and S. A. Chaudhry, Facile Fabrication of novel Y-doped ZnO biochar-based nanocomposite for efficient removal of Sulfasalazine, Congo red and Bismarck brown-R: Insight into adsorption performance and mechanism, *Surf. Interfaces*, 2025, **71**, 106817, DOI: 10.1016/j.surfin.2025.106817.

15 N. Nouj, M. R. Abelouah and M. Idbella, *et al.*, Unlocking the Full Potential of Agro-Waste Bio-Coagulants for Industrial Wastewater Treatment using pH-First Optimization, *Water, Air, Soil Pollut.*, 2026, **237**, 97, DOI: 10.1007/s11270-025-08729-x.

16 I. Hamed, F. Özogul and J. M. Regenstein, Industrial applications of crustacean by-products (chitin, chitosan, and chitooligosaccharides): A review, *Trends Food Sci. Technol.*, 2016, **48**, 40–50, DOI: 10.1016/j.tifs.2015.11.007.

17 P. Sharma, H. Kaur, M. Sharma and V. Sahore, A review on applicability of naturally available adsorbents for the removal of hazardous dyes from aqueous waste, *Environ. Monit. Assess.*, 2011, **183**, 151–195, DOI: 10.1007/s10661-011-1914-0.

18 S. Mahmood, A. Bi, S. Shukla, S. Husain, J. Prakash and S. A. Chaudhry, Synthesis of carbon quantum dots decorated titanium disilicide: a novel hybrid solar-driven photocatalyst for sustainable wastewater treatment, *J. Mater. Chem. A*, 2025, **13**(37), 31781–31801, DOI: 10.1039/D5TA02427G.

19 A. B. Hamou, S. Elamraoui, S. Escudero-Curiel, A. Chaoui, S. Farsad, A. Amjlef and N. El Alem, Enhancing surface area of HNO3-activated digestate-derived biochar for methylene blue adsorption: RSM-CCD optimization, DFT-MD calculations, and mechanistic study, *Appl. Surf. Sci.*, 2025, **709**, 163842, DOI: 10.1016/j.apsusc.2025.163842.

20 A. B. Hamou, A. Amjlef, N. Nouj, A. Chaoui, S. Farsad, F. Morlet-Savary and N. El Alem, Persulfate activation by Fe-rich biochar from sewage sludge digestate for organic pollutants removal: performance and superoxide radical role, *J. Environ. Manage.*, 2025, **390**, 126331, DOI: 10.1016/j.jenvman.2025.126331.

21 H. N. Tran, E. C. Lima, R. S. Juang, J. C. Bollinger and H. P. Chao, Thermodynamic parameters of liquid–phase adsorption process calculated from different equilibrium constants related to adsorption isotherms: A comparison study, *J. Environ. Chem. Eng.*, 2021, **9**(6), 106674, DOI: 10.1016/j.jece.2021.106674.

22 S. Li, Y. Gong, Y. Yang, C. He, L. Hu, L. Zhu, L. Sun and D. Shu, Recyclable CNTs/Fe$_3$O$_4$ magnetic nanocomposites as adsorbents to remove bisphenol A from water and their regeneration, *Chem. Eng. J.*, 2015, **260**, 231–239, DOI: 10.1016/j.cej.2014.09.032.

23 H. Hu, Y. Lin, B. Yang, X. Wen, P. Ma, X. J. Loh, Z. Luo, Z. Li and Y. L. Wu, Biomineralization-inspired functional biomaterials: From principles to practice, *Chem. Eng. J.*, 2025, **504**, 158624, DOI: 10.1016/j.cej.2024.158624.

24 I. Shahzadi, Y. Wu, H. Lin, J. Huang, Z. Zhao, C. Chen, X. Shi and H. Deng, Yeast biomass ornamented macro-hierarchical chitin nanofiber aerogel for enhanced adsorption of cadmium(II) ions, *J. Hazard. Mater.*, 2023, **453**, 131312, DOI: 10.1016/j.jhazmat.2023.131312.

25 B. Focher, A. Naggi, G. Torri, A. Cosani and M. Terbojevich, Structural differences between chitin polymorphs and their precipitates from solutions-evidence from CP-MAS sC.NMR, FT-IR and FT-Raman spectroscopy, *Carbohydr. Polym.*, 1992, **17**(2), 97–102.

26 K. Mohanrasu, A. C. Manivannan and H. J. R. Rengarajan, *et al.*, Eco-friendly biopolymers and composites: a sustainable development of adsorbents for the removal of pollutants from wastewater, *npj Mater. Sustain.*, 2025, **3**, 13, DOI: 10.1038/s44296-025-00057-9.

27 S. Kumari, P. Rath, A. Sri Hari Kumar and T. N. Tiwari, Extraction and characterization of chitin and chitosan from fishery waste by chemical method, *Environ. Technol. Innovation*, 2015, **3**, 77–85, DOI: 10.1016/j.eti.2015.01.002.

28 S. Kumari, S. H. Kumar Annamareddy, S. Abanti and P. Kumar Rath, Physicochemical properties and characterization

of chitosan synthesized from fish scales, crab and shrimp shells, *Int. J. Biol. Macromol.*, 2017, **104**, 1697–1705, DOI: 10.1016/j.ijbiomac.2017.04.119.

29 K. Suneeta, P. Rath and H. K. A. Sri, Chitosan from shrimp shell (Crangon crangon) and fish scales (Labeorohita): Extraction and characterization, *Afr. J. Biotechnol.*, 2016, **15**, 1258–1268, DOI: 10.5897/ajb2015.15138.

30 E. Muñoz and J. A. García-Manrique, Water absorption behaviour and its effect on the mechanical properties of flax fibre reinforced bioepoxy composites, *Int. J. Polym. Sci.*, 2015, **2015**(1), 390275, DOI: 10.1155/2015/390275.

31 H. S. Jung, M. H. Kim and W. H. Park, Preparation and Structural Investigation of Novel β-Chitin Nanocrystals from Cuttlefish Bone, *ACS Biomater. Sci. Eng.*, 2019, **5**, 1744–1752, DOI: 10.1021/acsbiomaterials.8b01652.

32 G. Cárdenas, G. Cabrera, E. Taboada and S. P. Miranda, Chitin characterization by SEM, FTIR, XRD, and ^{13}C cross polarization/mass angle spinning NMR, *J. Appl. Polym. Sci.*, 2004, **93**, 1876–1885, DOI: 10.1002/app.20647.

33 J. D. Goodrich and W. T. Winter, α-Chitin nanocrystals prepared from shrimp shells and their specific surface area measurement, *Biomacromolecules*, 2007, **8**, 252–257, DOI: 10.1021/bm0603589.

34 X. Liu, C. He, X. Yu, Y. Bai, L. Ye, B. Wang and L. Zhang, Net-like porous activated carbon materials from shrimp shell by solution-processed carbonization and H$_3$PO$_4$ activation for methylene blue adsorption, *Powder Technol.*, 2018, **326**, 181–189, DOI: 10.1016/j.powtec.2017.12.034.

35 H. El Knidri, R. El Khalfaouy, A. Laajeb, A. Addaou and A. Lahsini, Eco-friendly extraction and characterization of chitin and chitosan from the shrimp shell waste via microwave irradiation, *Process Saf. Environ. Prot.*, 2016, **104**, 395–405, DOI: 10.1016/j.psep.2016.09.020.

36 E. H. Cho and L. C. Lin, Nanoporous Material Recognition via 3D Convolutional Neural Networks: Prediction of Adsorption Properties, *J. Phys. Chem. Lett.*, 2021, **12**, 2279–2285, DOI: 10.1021/acs.jpclett.1c00293.

37 Z. Yu and D. Lau, Molecular dynamics study on stiffness and ductility in chitin–protein composite, *J. Mater. Sci.*, 2015, **50**, 7149–7157, DOI: 10.1007/s10853-015-9271-y.

38 S. M. Dadou, M. I. El-Barghouthi, S. K. Alabdallah, A. A. Badwan, M. D. Antonijevic and B. Z. Chowdhry, Effect of protonation state and N-acetylation of chitosan on its interaction with xanthan gum: A molecular dynamics simulation study, *Mar. Drugs*, 2017, **15**(10), 298, DOI: 10.3390/md15100298.

39 P. X. Pinto, S. R. Al-Abed and D. J. Reisman, Biosorption of heavy metals from mining influenced water onto chitin products, *Chem. Eng. J.*, 2011, **166**, 1002–1009, DOI: 10.1016/j.cej.2010.11.091.

40 B. Bolto and J. Gregory, Organic polyelectrolytes in water treatment, *Water Res.*, 2007, **41**, 2301–2324, DOI: 10.1016/j.watres.2007.03.012.

41 L. B. Escudero, P. Y. Quintas, R. G. Wuilloud and G. L. Dotto, Recent advances on elemental biosorption, *Environ. Chem. Lett.*, 2019, **17**, 409–427, DOI: 10.1007/s10311-018-0816-6.

42 O. Oprea, D. Gingasu, D. C. Culita, J. M. Calderon Moreno, G. Marinescu and S. Preda, A sustainable approach for the synthesis of magnesium aluminate spinel towards photocatalytic applications, *J. Mater. Sci.*, 2025, **97**, 1–21, DOI: 10.1007/s10853-025-10946-y.

43 A. Laghzal, M. H. Hmamou, B. Boudinar, N. Nouj, H. Ighnih, F. Salmoun and Y. Tligui, Valorizing Moroccan crab shells to purify water from Orange G dye: Exploring equilibrium, kinetics, and thermodynamics, *Desalin. Water Treat.*, 2024, **320**, 100738, DOI: 10.1016/j.dwt.2024.100738.

44 R. M. Jain, K. H. Mody, J. Keshri and B. Jha, Biological neutralization and biosorption of dyes of alkaline textile industry wastewater, *Mar. Pollut. Bull.*, 2014, **84**, 83–89, DOI: 10.1016/j.marpolbul.2014.05.033.

45 K. Rambabu, J. AlYammahi, G. Bharath, A. Thanigaivelan, N. Sivarajasekar and F. Banat, Nano-activated carbon derived from date palm coir waste for efficient sequestration of noxious 2,4-dichlorophenoxyacetic acid herbicide, *Chemosphere*, 2021, **282**, 131103, DOI: 10.1016/j.chemosphere.2021.131103.

46 A. Spoiala, C. I. Ilie, G. Dolete, A. M. Croitoru, V. A. Surdu, R. D. Truscă and L. M. Ditu, Preparation and characterization of chitosan/TiO$_2$ composite membranes as adsorbent materials for water purification, *Membranes*, 2022, **12**, 804, DOI: 10.3390/membranes12080804.

47 K. Rambabu, G. Bharath, F. Banat and P. L. Show, Biosorption performance of date palm empty fruit bunch wastes for toxic hexavalent chromium removal, *Environ. Res.*, 2020, **187**, 109694, DOI: 10.1016/j.envres.2020.109694.

48 A. Zakaria, J. Amane and E. A. Noureddine, Core–shell architecture based on bio-sourced porous carbon: The shape formation mechanism at the solid/liquid interface layer, *RSC Adv.*, 2019, **9**, 25544–25553, DOI: 10.1039/c9ra04869c.

49 M. Benafqir, Z. Anfar, M. Abbaz, R. El Haouti, S. Lhanafi, Y. Azougarh, A. Ait El Fakir, M. Ez-zahery and N. El Alem, Hematite–titaniferous sand as a new low-cost adsorbent for orthophosphates removal: Adsorption, mechanism and Process Capability study, *Environ. Technol. Innovation*, 2019, **13**, 153–165, DOI: 10.1016/j.eti.2018.10.009.

50 G. D. Değermenci, N. Değermenci, V. Ayvaoğlu, E. Durmaz, D. Çakır and E. Akan, Adsorption of reactive dyes on lignocellulosic waste; characterization, equilibrium, kinetic and thermodynamic studies, *J. Cleaner Prod.*, 2019, **225**, 1220–1229, DOI: 10.1016/j.jclepro.2019.03.260.

51 Y. Zhou, L. Ge, N. Fan and M. Xia, Adsorption of Congo red from aqueous solution onto shrimp shell powder, *Adsorpt. Sci. Technol.*, 2018, **36**, 1310–1330, DOI: 10.1177/0263617418768945.

52 K. Rambabu, G. Bharath, F. Banat, P. L. Show and H. H. Cocoletzi, Mango leaf extract incorporated chitosan antioxidant film for active food packaging, *Int. J. Biol. Macromol.*, 2019, **126**, 1234–1243, DOI: 10.1016/j.ijbiomac.2018.12.196.

53 P. Krishnamoorthy, D. G. Dixon, Z. Ren, N. Mora and C. W. Chao, Modeling the distribution of an adsorbing

solute in a catalyzed column, *Miner. Eng.*, 2022, **182**, 107556, DOI: 10.1016/j.mineng.2022.107556.

54 J. Chang, Z. Shen, X. Hu, E. Schulman, C. Cui, Q. Guo and H. Tian, Adsorption of Tetracycline by Shrimp Shell Waste from Aqueous Solutions: Adsorption Isotherm, Kinetics Modeling, and Mechanism, *ACS Omega*, 2020, **5**, 3467–3477, DOI: 10.1021/acsomega.9b03781.

55 A. Chaoui, A. Imgharn, A. C. Estrada, A. B. Hamou, S. Farsad, N. Nouj, M. Ez-zahery, T. Trindade, A. Albourine and N. E. Alem, Chromium(vi) remediation via biochar@-polyaniline composite: Advancing water treatment using biogas residue digestate, *Adv. Compos. Hybrid Mater.*, 2025, **8**(4), 312, DOI: 10.1007/s42114-025-01345-7.

56 R. Haounati, H. Ighnih, R. E. Malekshah, N. Nouj, H. Ouachtak, B. Šljukić and A. Ait Addi, Advanced contaminant removal through synergistic interactions of montmorillonite, $CoFe_2O_4$ nanoparticles, and surfactants: Combining theoretical and experimental approaches, *J. Mol. Liq.*, 2025, **428**, 127490, DOI: 10.1016/j.jcis.2008.08.066.

57 X. Q. Qiao, F. C. Hu, F. Y. Tian, D. F. Hou and D. S. Li, Equilibrium and kinetic studies on MB adsorption by ultrathin 2D MoS_2 nanosheets, *RSC Adv.*, 2016, **6**, 11631–11636, DOI: 10.1039/c5ra24328a.

58 N. El Messaoudi, A. El Mouden, M. El Khomri, A. Bouich, Y. Fernine, Z. Ciğeroğlu, J. H. P. Américo-Pinheiro, N. Labjar, A. Jada, M. Sillanpää and A. Lacherai, Experimental study and theoretical statistical modeling of acid blue 25 remediation using activated carbon from Citrus sinensis leaf, *Fluid Phase Equilib.*, 2022, **563**, 113585, DOI: 10.1016/j.fluid.2022.113585.

59 J. A. Rippon and D. J. Evans, Improving the properties of natural fibres by chemical treatments, *Handbook of Natural Fibres: Processing and Applications*, Elsevier Inc., 2020, vol. 2, pp. 245–321, DOI: 10.1016/B978-0-12-818782-1.00008-0.

60 A. Ben Hamou, M. Enneiymy, S. Farsad, A. Amjlef, A. Chaoui, N. Nouj, A. Majdoub, A. Jada, M. Ez-Zahery and N. El Alem, Novel chemically reduced cobalt-doped g-C_3N_4 (CoCN-*x*) as a highly heterogeneous catalyst for super-degradation of organic dyes via peroxymonosulfate activation, *Mater. Adv.*, 2024, **5**(5), 1960–1976, DOI: 10.1039/D3MA00818E.

61 A. Chaoui, S. Farsad, A. Ben Hamou, A. Amjlef, N. Nouj, M. Ezzahery and N. El Alem, Reshaping environmental sustainability: Poultry by-products digestate valorization for enhanced biochar performance in methylene blue removal, *J. Environ. Manage.*, 2024, **351**, 119870, DOI: 10.1016/j.jenvman.2023.119870.

62 V. T. Le, M. U. Dao, H. S. Le, D. L. Tran, V. D. Doan and H. T. Nguyen, Adsorption of Ni(ii) ions by magnetic activated carbon/chitosan beads prepared from spent coffee grounds, shrimp shells and green tea extract, *Environ. Technol.*, 2020, **41**, 2817–2832, DOI: 10.1080/09593330.2019.1584250.